Advanced Ceramics Progress: Vol. 11, No. 2, (Spring 2025) 12-23

Materials and Energy Research Center
MERC

Contents lists available at ACERP

Advanced Ceramics Progress

Journal Homepage: www.acerp.ir

Original Research Article

Tuning Bioactivity and Degradation Behavior of Magnesium Implants Using Wollastonite Embedded Plasma Electrolytic Oxidation Coatings

Mahya Karimi [a], Benyamin Yarmand [b]*, Mohammad Javad Eshraghi [c]

[a] *MSc Student, Department of Nanotechnology and Advanced Materials, Materials and Energy Research Center, Karaj, Iran.*
[b] *Associate Professor, Department of Nanotechnology and Advanced Materials, Materials and Energy Research Center, Karaj, Iran.*
[c] *Associate Professor, Department of Semiconductors, Materials and Energy Research Center, Karaj, Iran.*

* Corresponding Author Email: byarmand@merc.ac.ir (B. Yarmand) URL: https://www.acerp.ir/article_227750.html

ARTICLE INFO

Article History:
Received 14 June 2025
Received in revised form 19 July 2025
Accepted 18 August 2025

Keywords:
Plasma Electrolytic Oxidation,
Magnesium,
Wollastonite,
Bioactivity,
Degradation

ABSTRACT

Magnesium alloys used as biodegradable implants require enhanced bioactivity and corrosion resistance in physiological media. This study investigated the bioactivity and degradation behavior of plasma electrolytic-oxidized magnesium coatings incorporating various amounts of biocompatible wollastonite particles. The findings revealed that the presence of wollastonite particles interfered with layer formation interactions which consequently led to a decrease in the formation voltage, a reduction in the oxide layer thickness, and an increase in the surface roughness. The incorporation of wollastonite particles into the oxide layer induced more calcium phosphate deposition during immersion in simulated body fluid, indicating enhanced bioactivity. Biodegradation evaluation revealed that the corrosion rate of the oxide layer increased from 0.588 to 3.229 mm.year^{-1} with the addition of 4.5 g.L^{-1} wollastonite particles, which resulted from the reduction in the structural compaction as indicated by electrochemical impedance spectroscopy. Therefore, wollastonite particles are a suitable additive to improve the bioactivity of plasma electrolytic-oxidized magnesium coatings that can provide a degradation rate suitable for biological media.

https://doi.org/10.30501/acp.2025.530383.1179

1. INTRODUCTION

Biodegradable implants are a basic requirement for bone tissue engineering since they can meet the functional and biomechanical needs of injured individuals during bone regeneration. The main advantage of biodegradable implants over permanent ones is the elimination of secondary surgery, which imposes special necessities on design, material selection, and fabrication. Among them, these implants must have excellent biocompatibility to provide proper integration with bone tissue post-implantation and prevent inflammation. They must also withstand loads and prevent from transferring stress to the healing bone tissue. After bone regeneration, they should be metabolized uniformly at an appropriate rate within the body so as not to cause toxicity (Radha & Sreekanth, 2017; Seetharaman et al., 2023; Witte, 2015).

Magnesium-based biomaterials are among the most promising choices for manufacturing biodegradable implants. Magnesium alloys offer orthopedic implants due to their bone-like biomechanical properties that can effectively reduce the stress-shielding effect. The superior biocompatibility of these biometals compared to stainless steel or titanium alloys is another key feature

Please cite this article as: Karimi, M., Yarmand, B. & Eshraghi, M. J. (2025). Tuning Bioactivity and Degradation Behavior of Magnesium Implants Using Wollastonite Embedded Plasma Electrolytic Oxidation Coatings, *Advanced Ceramics Progress*, 11(2), 12-23. https://doi.org/10.30501/acp.2025.530383.1179

2423-7485/© 2025 The Author(s). Published by MERC.
This is an open access article under the CC BY license (https://creativecommons.org/licenses/by/4.0/).

that supports their application in orthopedics. However, their high degradation rate in physiological environments remains a major limitation. Rapid degradation of biodegradable implants may cause premature weakening of mechanical properties before complete bone regeneration occurs. Moreover, the rapid release of hydroxyl ions and hydrogen gas may disrupt the normal functioning of the patient's body (Fattah-alhosseini et al., 2022; Waizy et al., 2013; Yang et al., 2024).

One approach that has recently attracted significant attention is the surface modification of magnesium alloys using Plasma Electrolytic Oxidation (PEO) technology. The performance of this technique in improving the biocompatibility and degradation resistance of magnesium in the body environment holds great promise in the development of biodegradable implants. During the PEO process, a uniform adhesive ceramic coating forms across the entire implant surface through oxidation at voltages above the dielectric breakdown threshold. This coating can act as a barrier against the destructive medium. The surface of the PEO coating is inherently porous and provides desirable morphology for cellular interactions. A main advantage of this method in medical applications is the ability to enhance the biological activity and biocompatibility of the implant surface by incorporating biocompatible compounds into the PEO coating. The promoted biological features can be easily induced into the ceramic coating by adding beneficial compounds to the electrolyte (Fattah-alhosseini et al., 2022; Hussein et al., 2012; Mohedano et al., 2018; Yang et al., 2024).

Bioabsorbable materials are suitable candidates for introducing new biological properties to PEO-coated magnesium because they gradually decompose in the human body and can be replaced by newly formed bone tissue. Wollastonite, a calcium silicate, has superior biological activity and beneficial physicochemical properties. This compound can be partially dissolved in body fluids, causing the release of calcium ions and the formation of Si–OH groups. These promote apatite nucleation and growth, thus contributing to bone formation. In addition, they promote cell proliferation and differentiation, as well as facilitate integration with the existing bone tissue. Silicon also stimulates intercellular responses and plays an essential role in bone tissue formation and collagen mineralization (Joo & Choe, 2025; Sedelnikova et al., 2016).

The effect of wollastonite on the properties of PEO coatings has been studied to a limited extent. S.Y. Joo et al. prepared wollastonite-forsterite composite coatings containing Mn as a secondary layer on the plasma electrolytic oxidized Ti-6Al-4V alloy via spin coating and studied their bioactivity and corrosion properties (Joo & Choe, 2025). M.B. Sedelnikova et al. created wollastonite and calcium phosphate biocoatings without/with Zn- and Cu-incorporation on commercially pure titanium using PEO at different voltages and investigated their physical properties (Sedelnikova et al., 2016). In another research, they examined the corrosion behavior of Mg0.8Ca alloy surface modified by wollastonite micro-arc coatings at various voltages (Sedelnikova et al., 2021). Hence, finding out how and to what extent wollastonite particles affect the properties of PEO-coated magnesium could be valuable for bone tissue engineering.

This study aimed to investigate the effect of wollastonite particles on the bioactivity and degradation behavior of PEO-coated magnesium simultaneously to develop a simple and low-cost solution for temporary implants. In this regard, the synthesized wollastonite particles were incorporated at the maximum possible concentration into the ceramic coating formed on the magnesium substrate during the PEO process. Then, their effect on the growth of the ceramic layer as well as the formation of crystalline phases, bioactivity, and corrosion protection performance was studied.

2. MATERIALS and METHODS

2.1. Synthesis of Wollastonite Particles

Wollastonite particles were synthesized using the sol-gel process. For this purpose, 4.7 mL of tetraethyl orthosilicate ($Si(OC_2H_5)_4$, Merck) was added dropwise to 75 mL of 0.2 N aqueous hydrochloric acid (HCl, Merck). After homogenization, 27.5 g of calcium nitrate ($Ca(NO_3)_2.7H_2O$, Merck) was slowly added and stirred for 24 h at room temperature to form a gel. The resulting gel was dried in an oven at 100 °C for 12 h. Then, it was ground into powder and heated at 800 °C for 3 h to achieve crystallization.

2.2. Coating Conditions

Coatings were performed using the PEO process on commercially pure magnesium ingot. First, pieces with the dimensions of 20×10×2 mm^3 were cut from magnesium ingot, then sanded and polished with silicon carbide emery paper up to 2000 grit. Afterward, they were degreased with ethanol, dried in hot air, and finally stored in a desiccator. The PEO treatment was applied by a 6-kW direct pulse power supply with a frequency of 1000 Hz. The positive pole (anode) was connected to the magnesium substrate, and the negative pole (cathode) to a stainless-steel container with a water-circulating cooling system. The coating process was conducted at a current density of 50 $mA.cm^{-2}$ with a duty cycle of 33% for 7 min. The basic electrolyte was prepared by dissolving 5 $g.L^{-1}$ sodium phosphate ($Na_3PO_4.12H_2O$, Merck) and 2 $g.L^{-1}$ potassium hydroxide (KOH, Merck) in distilled water. To incorporate wollastonite particles, 1.5, 3, and 4.5 $g.L^{-1}$ of the synthesized particles were added to the basic electrolyte, and the mixture was and homogenized by stirring and ultrasonication. The specifications of the electrolyte and the labeled samples are presented in Table 1.

TABLE 1. The specifications of the electrolytes and samples

Sample	Na_3PO_4 ($g.L^{-1}$)	KOH ($g.L^{-1}$)	Wollastonite particles ($g.L^{-1}$)	Conductivity ($mS.cm^{-1}$)	pH
W0	5	2	0	5.80	13.1
W1.5	5	2	1.5	6.10	13.2
W3	5	2	3	7.12	13.4
W4.5	5	2	4.5	8.17	13.6

2.3. Characterization

The crystalline structures and chemical bonds formed in the synthesized particles and the PEO coatings were identified using X-Ray Diffraction (XRD, Philips PW3710 with Cu Kα radiation of 0.154056 nm) and Fourier Transform Infrared Spectroscopy (FTIR, Bruker Vector 33). The microstructure and chemical composition of the samples were examined using a Field Emission Scanning Electron Microscope (FESEM, Tescan Mira III) and an Energy Dispersive Spectrometer (EDS, Oxford INCA energy 300). The zeta potential of the particles was measured via the Zeta potential analyzer (Horiba SZ100). The thickness of the coatings was determined using a Phynix FN thickness gauge by averaging measurements taken at several points. The surface roughness was evaluated using a Time Group TR100 gauge, with multiple measurements conducted in both longitudinal and transverse directions.

2.4. In-vitro Bioactivity Test

The bioactivity of the PEO coatings was determined by incubating the samples in Simulated Body Fluid (SBF) for 14 days under dynamic conditions at 37 °C. The SBF was refreshed every other day. It was prepared according to Kukubo's method by dissolving specified amounts of reagents (NaCl, $NaHCO_3$, KCl, $K_2HPO_4.3H_2O$, $MgCl_2.6H_2O$, $CaCl_2$, Na_2SO_4, and $CH_2OH)_3CNH_2$ in deionized water at 37 °C, and then buffered to pH=7.4 using diluted HCl. All chemicals were purchased from Merck.

2.5. Corrosion Studies

The corrosion protection performance of the samples was evaluated using a potentiostat EG & G, Princeton Applied Research 263A, in SBF at 37 °C. To stabilize the open circuit potential, the samples with an active area of 1 cm^2 were immersed in SBF for 6 h. The measurements were performed by a three-electrode cell, in which the sample served as the working electrode, a platinum wire as the counter electrode, and saturated calomel as the reference electrode. The Potentiodynamic polarization test was conducted by applying a potential from −600 to +600 mV relative to the open circuit potential at a sweep rate of 1 $mV.s^{-1}$. Electrochemical Impedance Spectroscopy (EIS) was carried out by applying an AC signal with an amplitude of ±10 mV relative to the open circuit potential in the frequency range of 0.01 Hz to 100 kHz.

3. RESULTS and DISCUSIONS

3.1. Characterization of Wollastonite Particles

The characteristics of the crystalline phase, chemical bonds, and microstructure of the synthesized particles are shown in Figure 1. Identification of the diffracted peaks in the XRD pattern (Figure 1a) indicates that wollastonite is formed, based on JCPDS card number 27-0088, according to the labeled indices. In addition, peaks related to other compounds or different stoichiometries are not detected. Chemical bond characterization using the FTIR spectrum (Figure 1 b) reveals that the absorption band located at 435 cm^{-1} corresponds to the Ca−O bond. Absorption bands related to the O−Si−O bond appear at 564 cm^{-1} and 717 cm^{-1}. The Si−O bond is centered at 939 cm^{-1}. Absorption bands corresponding to the Si−O−Si bond emerge at 988 cm^{-1} and 1068 cm^{-1}. Moreover, H−O−H and O−H absorption bands, attributed to moisture absorption, are observed at 1638 cm^{-1} and 3431 cm^{-1}. Therefore, it can be concluded that the wollastonite particles were successfully synthesized using the sol-gel process and fully crystallized during heating at 800 °C for 3 h. The FESEM image in Figure 1c confrms that the wollastonite particles do not have a specific morphology and generally possess sharp corners with varying dimensions. The EDS analysis presented in Figure 1d further confirms the formation of wollastonite particles. Measurement of the wollastonite surface charge in an aqueous medium with pH 13, similar to basic electrolyte conditions, reveals a zeta potential of about -17.9 mV. The negative surface charge may be attributed to oxygen species on the surface of wollastonite particles, which prevents their agglomeration and maintains their dispersion in the alkaline electrolyte. This indicates a suitable distribution and stability of wollastonite particles during the PEO layer growth interactions (Joo & Choe, 2025; Sedelnikova et al., 2021).

3.2. Coating Growth Mechanism

The growth of the PEO coating on the magnesium substrate and its influence on wollastonite particles were investigated by examining the responding voltage changes during the process. Figure 2 presents the graphs of the responding voltage as a function of oxidation time, along with the extracted breakdown and final voltages. It can be seen that all the curves follow the same trend throughout the process. In the first stage, during anodizing, the responding voltage increases rapidly with a steep slope.

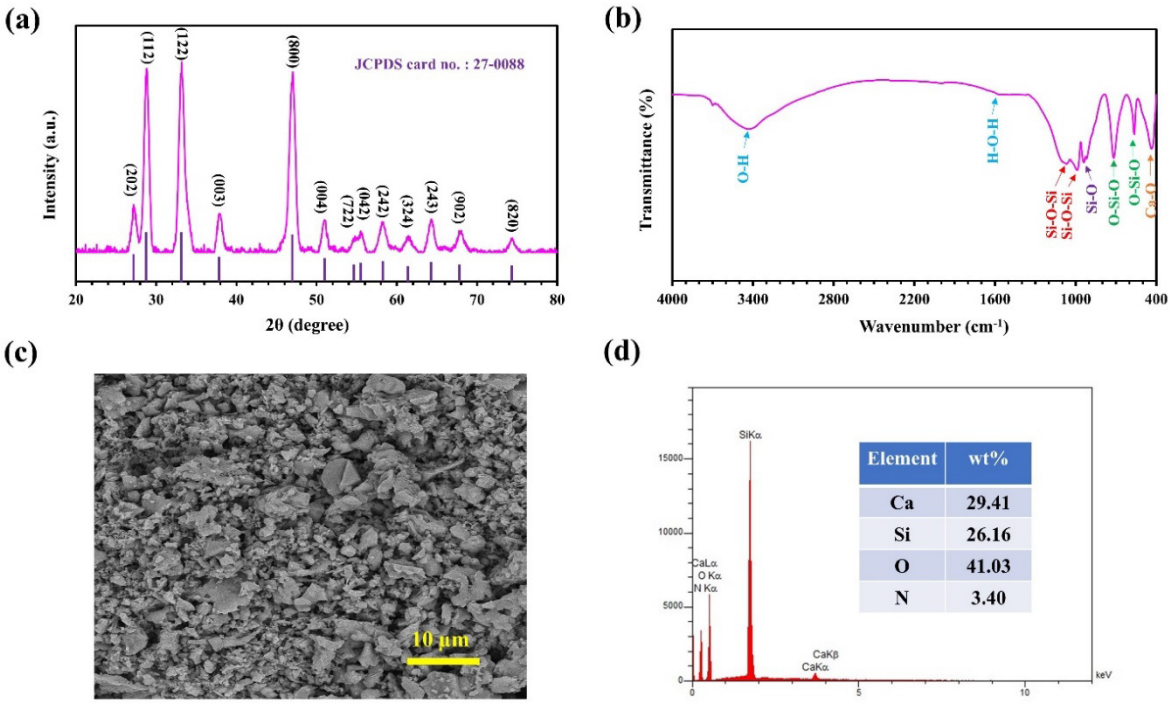

Figure 1. (a) XRD pattern, (b) FTIR spectrum, (c) FESEM image, and (d) EDS spectrum of wollastonite particles

This results from the reaction of magnesium cations with accumulated hydroxyl anions at the interface between the substrate and the electrolyte, producing a passive oxide layer. As this passive layer thickens, its electrical resistance increases, causing a rise in the responding voltage at the applied constant current density. The darkening of the substrate surface and the emission of gas bubbles confirm the formation of the passive layer during anodizing. This stage continues until the oxygen anions pass through the passive layer to complete the electric current cycle. As ion diffusion becomes more difficult, oxygen anions accumulate at the interface of the passive layer and the electrolyte, hence an increase in the electrical potential. When the potential exceeds the dielectric breakdown threshold, electrical discharges occur on the surface of the passive layer, triggering an electron avalanche into the conduction band of the forming layer. From this moment onward, the layer growth mechanism proceeds through simultaneous occurrence of anodizing and sparking. This stage is characterized by a decrease in the slope of the responding voltage curve, which results from an increased contribution of the electron flow from the sparks to the electric current cycle. At this stage, tiny white sparks appear on the sample surface, gradually covering it completely. As the process continues, the yellowish sparks become stronger and more stably on the layer surface. This stability is reflected in the responding voltage changes, which then shows an almost constant slope. During this stage, the oxide layer grows by the Micro-Arc Oxidation (MAO) mechanism, in which the materials formed on the layer surface melt due to successive electrical discharges and then freeze in contact with the cold electrolyte. This process continues until the end of the treatment (Yerokhin et al., 2000).

Addition of wollastonite particles causes the oxide layer to form at lower voltages, as observed from the breakdown and final voltages given in Figure 2.

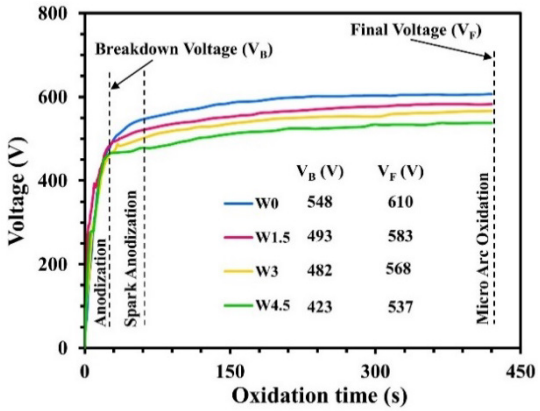

Figure 2. Variations of responding voltage versus oxidation time

This phenomenon may result from the increased conductivity of the electrolyte due to the presence of wollastonite particle addition, rising the conductivity from 5.80 $mS.cm^{-1}$ to 8.17 $mS.cm^{-1}$. The conductivity of the electrolyte suspension is affected by the concentration, type, and surface charge of the additives. These factors affect the mechanism of oxide layer

growth, given the electrochemical nature of the process. According to the Ikonopisov relationship, upon increasing the electrolyte conductivity, the potential at the interface between the electrolyte and the oxide layer increases due to the accumulation of electrical charges. This facilitates the onset of electron avalanche (Erfanifar et al., 2017; Ikonopisov, 1977).

3.3. Morphology of Coatings

Figure 3 illustrates the FESEM images and EDS spectra of the PEO coatings' surface. The surface of all the samples exhibits a crater-like microstructure, which is typical of the discharge channels formed during the MAO stage. This morphology results from the ejection of molten material from these channels during spark generation. Upon contact with the electrolyte, the molten material spreads across the surface and rapidly solidifies. The presence of gas and the rapid cooling at the interface between the sample and the electrolyte are the primary causes of pore formation. This microstructure provides favorable conditions for implant integration by offering multiple sites for mechanical interlocking with the surrounding bone tissue. Addition of wollastonite particles does not significantly change the surface morphology. Only in W4.5, which contains higher additives, is a greater accumulations of particles within the pores (Dehnavi et al., 2015; Yerokhin et al., 2002).

The EDS results of the samples' surface (Figure 3) indicate that magnesium and oxygen dominate the chemical composition of the coatings, confirming the successful oxidation of the magnesium substrate. In addition, some phosphorus is present, likely due to the incorporation of phosphate anions from the electrolyte during layer formation under harsh conditions of the MAO process. This presence can improve bioactivity. In W1.5, W3, and W4.5, silicon and calcium are added to the previous elements, with their maximum values found in W4.5. This proves that the wollastonite particles are well incorporated into the microstructure of the oxide layer. The distribution of wollastonite particles within the layer was further investigated by EDS mapping from W4.5, as demonstrated in Figure 4.

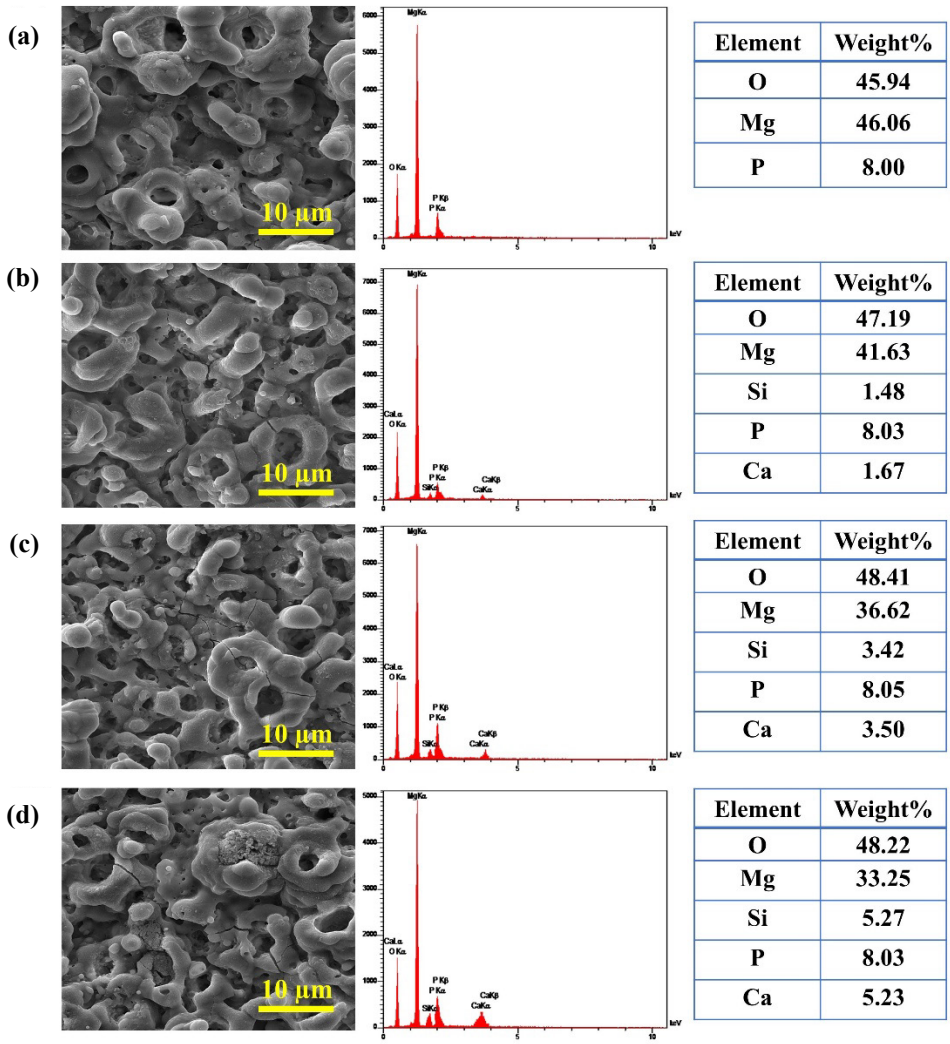

Element	Weight%
O	45.94
Mg	46.06
P	8.00

Element	Weight%
O	47.19
Mg	41.63
Si	1.48
P	8.03
Ca	1.67

Element	Weight%
O	48.41
Mg	36.62
Si	3.42
P	8.05
Ca	3.50

Element	Weight%
O	48.22
Mg	33.25
Si	5.27
P	8.03
Ca	5.23

Figure 3. FESEM images and EDS spectra of (a) W0, (b) W1.5, (c) W3, and (d) W4.5

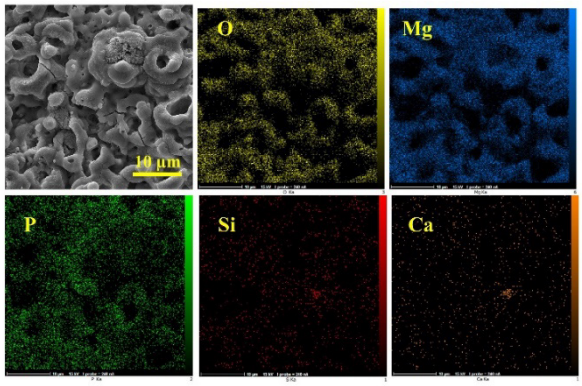

Figure 4. EDS maps from the W4.5 surface

Silicon and calcium are uniformly distributed across the entire surface, indicating a uniform distribution of wollastonite particles. Besides, a few silicon- and calcium-rich spots are visible, suggesting the presence of wollastonite agglomerations. To study the growth of the PEO coatings, FESEM images of the samples' cross-sections are presented in Figure 5.

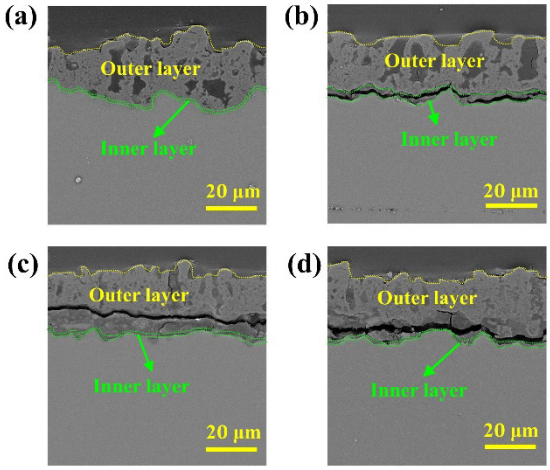

Figure 5. FESEM images from cross-sections of (a) W0, (b) W1.5, (c) W3, and (d) W4.5

The coatings display a wavy and non-planar interface with the substrate, likely caused by the non-equilibrium dissolution of the substrate during the MAO process. This may result from the harsh processing conditions or high reactivity of magnesium under oxidation. The PEO coating in W0 exhibits good adhesion strength to the substrate. In contrast, in the other samples, it has detached during preparation for imaging, which may be due to embrittlement resulting from the presence of wollastonite particles. The inherent defects of the MAO process are also visible in the cross-section images. Besides, the high surface roughness of the coatings can be observed. The thickness of the PEO coatings is estimated to be approximately 15 to 30 µm. The bilayer microstructure of the oxide layer is also evident. The inner part, formed directly on the substrate during the early stages of the process, is thin and has few structural defects. The outer part, resulting from repeated eruption of molten materials and rapid solidification, has greater inherent defects and increased thickness (Erfanifar et al., 2017). Incorporating wollastonite particles into the PEO coating can be attributed to their negative surface charge, making them to move toward the substrate under the influence of electrophoretic forces. These particles are attracted to the oxide layer, particularly at sites with high surface energy. They become trapped and embedded in the molten material during MAO interactions, including perturbation and fluctuation. The frequent occurrence of sparks on the coating surface facilitates better movement and integration of wollastonite particles. Generally, a higher particle population provides more incorporation. Given the uniform distribution of silicon and calcium elements throughout the coating and the lower melting point of wollastonite particles (approximately 1540 °C) compared to that of the MgO matrix phase (2850 °C), it can be expected that they are partly reactively incorporated into the coating. Uniform coating compositions offer better biological properties (Gnedenkov et al., 2015; Lu et al., 2016).

3.4. Thickness and Surface Roughness of Coatings

The variations in the thickness and surface roughness of the PEO coatings, measured by the gauge, are presented in Figure 6. Upon adding wollastonite particles, the thickness of the PEO coating decreases, ranging from 28.1 µm in W0 to 17.3 µm in W4.5. In contrast, the surface roughness shows a reverse trend increases from 0.56 µm in W0 to 1.37 µm in W4.5. The reduction in the PEO coating thickness can be due to the effect of wollastonite particles on reducing the layer formation voltage in the MAO stage, as observed in the voltage response diagrams in Figure 2. The accumulation of wollastonite particles participates in the oxide layer in MAO interactions and absorbs the heat released by the sparks. Therefore, due to the high specific heat capacity of wollastonite, a smaller volume of oxide materials can melt and contribute to layer growth. This leads to a decrease in the growth rate, which is exacerbated by more wollastonite particles. Moreover, the presence of wollastonite particles disturbs the spark conditions, which become visible on the sample surface during the final half of the process. This phenomenon results from the high zeta potential of wollastonite particles, leading to their mass adsorption at inherent defects. Furthermore, the high reactivity of magnesium cations in anodic reactions as well as the low melting point of the magnesium substrate or wollastonite may also contribute. These factors might explain the increase in surface roughness, which has been reported in similar studies conducted on silica particles (Chen et al., 2024; Krishtal et al., 2015; Xu & Shen, 2019).

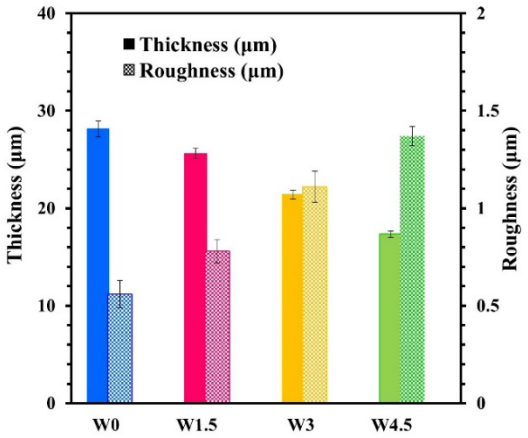

Figure 6. Thickness and surface roughness of the samples

3.5. Crystalline Phases

The XRD Patterns of W0 and W4.5 are given in Figure 7. In both samples, the peaks diffracted at 32.2°, 34.4°, 36.7°, 47.9°, 68.7°, and 70.1° corresponds to the (100), (002), (101), (102), (112), and (201) planes of magnesium, respectively, according to JCPDS card number 35-0821.

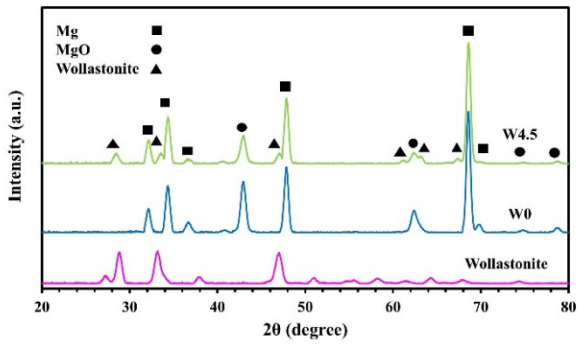

Figure 7. XRD patterns of wollastonite particles, W0, and W4.5

These peaks appear due to the penetration of X-rays through the PEO coating. The peaks at 42.9°, 62.3°, 74.7°, and 79.2° correspond to the (200), (220), (311), and (222) planes of magnesium oxide according to JCPDS card number 45-0946. This confirms the formation of a well-structured oxide layer as a result of the oxidation of the magnesium substrate during the MAO process, according to the reactions 1-4. In W4.5, all the aforementioned peaks appear but with reduced intensity. The decrement in the intensity of the magnesium peaks may result from increased X-ray absorption by the composite oxide layer. Similarly, the lower intensity of the oxide layer peaks may be due to the reduced thickness or amorphous structure of the PEO coating. In addition, wollastonite-related peaks appear at 27.5°, 33.2°, 47.2°,61.7°,64.3°, and 68.2°, which correspond to the (202), (122), (800), (324), (243), and (902) planes, respectively, based on JCPDS card number 27-0088. This indicates that the wollastonite particles are incorporated into the PEO coating. Their low intensity likely reflects the smaller amount of wollastonite particles present compared to the dominant MgO phase (Joo & Choe, 2025; Sedelnikova et al., 2016).

$$Mg \rightarrow Mg^{2+} + 2e^{-} \quad (1)$$

$$4OH^{-} \rightarrow O_2 + 2H_2O + 4e^{-} \quad (2)$$

$$Mg^{2+} + 2OH^{-} \rightarrow Mg(OH)_2 \quad (3)$$

$$Mg(OH)_2 \rightarrow MgO + H_2O \quad (4)$$

3.6. Bioactivity Analysis

To evaluate the bioactivity, the samples were immersed in SBF at 37 °C for 14 days. Figure 8 demonstrates FESEM images of the samples' surface along with EDS analysis. On W0, a thin layer of precipitates is deposited over the entire surface, but the pores of the PEO coating are still visible. The EDS results indicate that the precipitates are deficient calcium-phosphate compounds. On the surface of W1.5 to W4.5, higher amounts of calcium phosphate are deposited, thus forming a thick layer consisting of aggregates. The deposited layer is cracked due to the large amount of calcium-phosphate precipitates or dehydration during preparation. The amount of calcium and phosphorus on the surface of W4.5 is almost twice that of W0, indicating the valuable effect of the incorporated wollastonite particles on enhancing the surface bioactivity of the PEO coating. The precipitation of calcium phosphate compounds on W0 results from partial hydrolysis of the MgO layer during immersion in SBF. Due to the reaction of the oxide layer with the aqueous solution, numerous negatively charged Mg–OH bonds are formed at different sites, especially at inherent defects with higher surface energy. The accumulation of multiple local negative charges on the surface of the oxide layer makes the calcium cations of SBF electrostatically attracted to these areas and induces zones with positive charge. Then, to establish medium stability, phosphate and hypophosphate ions with opposite surface charges are attracted to these and create supersaturated regions of calcium and phosphorus. These regions, in contact with the oxide layer, facilitate the precipitation of calcium-phosphate nuclei and then their growth. Wollastonite particles in the MgO layer may enhance the ionic activity and nucleation of calcium phosphate compounds by releasing calcium cations according to reaction 5. Wollastonite has a high dissolution rate, and its partial dissolution in SBF disturbs the equilibrium of the supersaturated microenvironment in contact with the PEO layer, facilitating and accelerating the nucleation and growth of deposits.

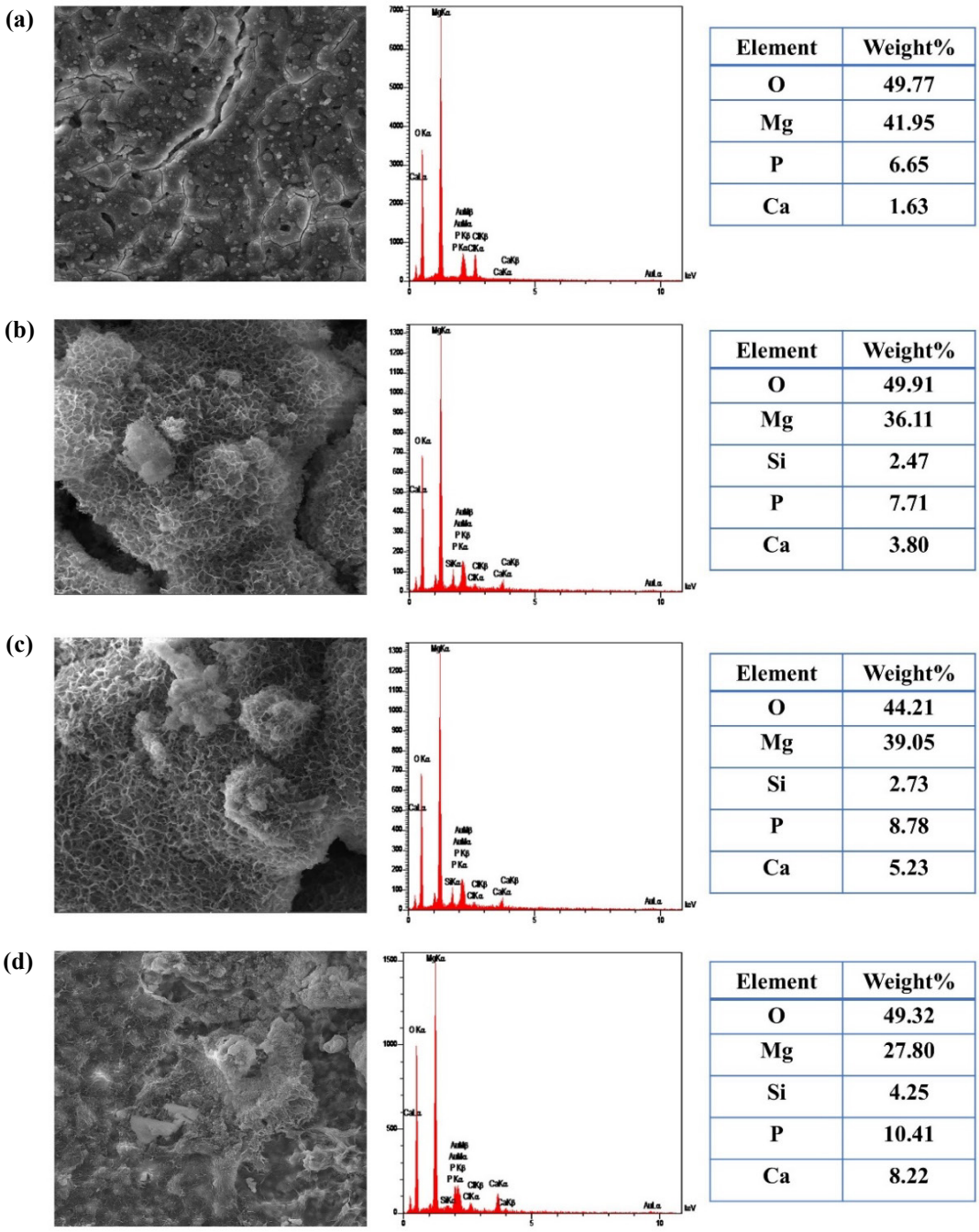

Element	Weight%
O	49.77
Mg	41.95
P	6.65
Ca	1.63

Element	Weight%
O	49.91
Mg	36.11
Si	2.47
P	7.71
Ca	3.80

Element	Weight%
O	44.21
Mg	39.05
Si	2.73
P	8.78
Ca	5.23

Element	Weight%
O	49.32
Mg	27.80
Si	4.25
P	10.41
Ca	8.22

Figure 8. FESEM images and EDS spectra of (a) W0, (b) W1.5, (c) W3, and (d) W4.5 after 14 days immersion in SBF

In addition, the hydrolysis of the silicon ions from the embedded wollastonite in contact with SBF can produce silicate gels that bind to hypophosphate ions by a neutralization reaction. This causes calcium cations to bind to their free chains to stabilize and form complex compounds rich in calcium and phosphate ions. These compounds promote the growth of further calcium phosphate deposits. Higher concentrations of incorporated wollastonite particles favorably improve bioactivity (Bordbar-Khiabani et al., 2019; Joo & Choe, 2025).

$$CaSiO_3 + H_2O \rightarrow Ca^{2+} + HSiO_3^- + OH^- \quad (5)$$

The biodegradation of the PEO coatings was investigated by monitoring the acidity of the biological medium. Figure 9 exhibits the changes in the pH of SBF at 37 °C over 14 days.

The pH changes follow a similar trend, initially increasing sharply and then stabilizing. In W0, the pH rises at a lower rate than the others, increasing from 7.4 to 9.2 after 8 days, followed by slight fluctuations until

the end. The samples containing wollastonite particles show more pH changes in shorter times. W4.5 experiences the highest rate of increase, reaching a pH of 9.7 after 6 days and then stabilizing. The pH increment after immersion results from the reaction of the PEO coating with the SBF, leading to the production of $Mg(OH)_2$. As the reactions progress, more degradation products cover the sample surface, which delays further degradation and results in pH stability. W0 exhibits a weaker chemical dissolution than the others due to the stable chemical composition of MgO, thus showing the least pH variations. By embedding biodegradable wollastonite particles within the MgO layer, the surface reactivity increases, leading to faster reaction with SBF and more severe pH changes. Overall, the presence of wollastonite particles accelerates the biodegradation of the MgO layer (Sedelnikova et al., 2016).

3.7. Corrosion Studies

The corrosion behavior of the samples was investigated by potentiodynamic polarization testing in SBF at 37 °C. The polarization curves of the samples are presented in Figure 10. The corrosion characteristics estimated from the curves in the Tafel region, along with the polarization resistance (R_p) and corrosion rate (C_R) calculated from the following equations (Stern, M., 1957), are given in Table 2.

$$R_p = \frac{\beta_a \times \beta_c}{2.3 \times i_{corr} \times (\beta_a + \beta_c)} \quad (6)$$

$$C_R(mm.year^{-1}) = 22.85 \times i_{corr}(mA.cm^{-2}) \quad (7)$$

where icorr is the corrosion current density, and β_a and β_c represent the anodic and cathodic slopes in the Tafel region, respectively. All the curves are free of oscillations, indicating that the PEO coatings maintain good stability in SBF. A comparison of polarization curves reveals that the protective performance of the PEO coatings is weakened by the incorporation of wollastonite particles. The corrosion potential of the samples follows a decreasing trend, suggesting an acceleration in their thermodynamic tendency for dissolution in SBF. Furthermore, the anodic branch of all the curves shifts towards higher current densities, indicating an increment in the kinetics of the degradation reactions. W0 has a corrosion rate of 0.588 mm.year^{-1}, which reaches 3.229 mm.year^{-1} in W4.5 with the embedment of wollastonite particles. The polarization resistance shows a decreasing trend, from 1.322 to 0.254 kΩ.cm² in W0 to W4.5, respectively.

The corrosion behavior of the PEO coating is the result of two main phenomena: resistance of the layer to the penetration of corrosive agents from the SBF toward the substrate interface, and prevention of the outward diffusion of dissolved magnesium ions.

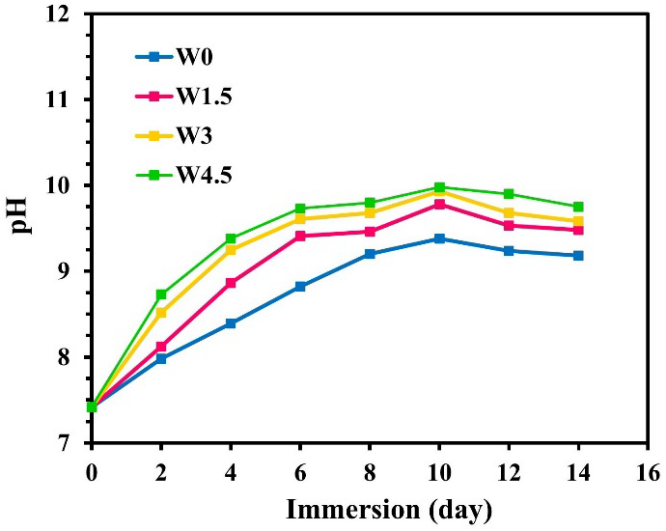

Figure 9. Changes in the pH value of SBF during 14 days of immersion

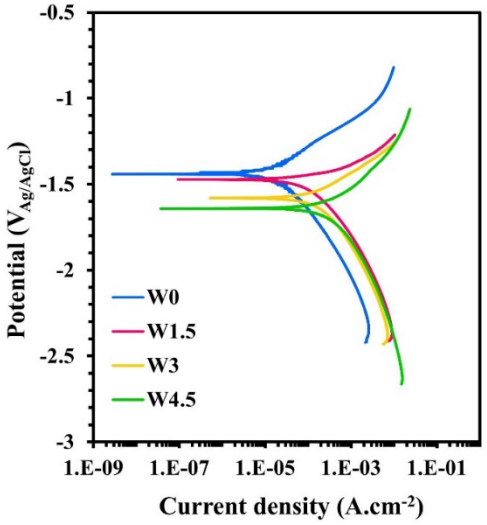

Figure 10. Potentiodynamic polarization curves of the specimens

TABLE 2. The corrosion parameters derived from potentiodynamic polarization curves

Sample	E_{corr} (V)	i_{corr} (μA.cm^{-2})	β_c (mV.dec^{-1})	β_a (mV.dec^{-1})	C_R (mm.year^{-1})	R_p (kΩ.cm²)
W0	-1.44	25.76	185	136	0.588	1.322
W1.5	-1.48	65.75	267	114	1.502	0.528
W3	-1.56	70.40	248	126	1.608	0.516
W4.5	-1.60	141.32	253	123	3.229	0.254

These are affected by factors such as surface roughness, coating thickness, and solubility of the oxide coating. Enhancing the surface roughness effectively increases the surface sites on the PEO coating for the adsorption of various corrosive ions from the SBF, thereby allowing them to penetrate the magnesium substrate more strongly. The reduction in the thickness of the PEO coating due to the incorporation of wollastonite particles shorten the distance and ease the penetration into the oxide layer, leading to a slight reduction in the protective power of the PEO coating. The greater solubility of the PEO coating caused by the presence of degradable wollastonite particles can also weaken the protective performance. In general, all these factors synergistically weaken the corrosion resistance of the samples (Bai & Chen, 2011; Venkateswarlu et al., 2012).

The effect of wollastonite particles on the properties of the PEO coating was studied using EIS. The Nyquist, Bode modulus, and Bode phase curves of all samples are shown in Figure 11. All Nyquist curves are arc-shaped, indicating the dominance of the charge transfer mechanism at the interface of the PEO coating and the SBF in controlling the degradation kinetics. W0 has the largest curve diameter and decreases with the placement of wollastonite particles in the PEO coating, reaching its smallest value at W4.5. This trend indicates increased permeability of the PEO coating. In the Bode modulus curves, W0 shows the highest impedance modulus at low frequencies and decreases with the incorporation of wollastonite particles.

The EIS data were analyzed with the equivalent circuit shown in Figure 11d. This circuit is constructed between the reference and working electrodes based on the bilayer microstructure of the PEO coating and the variations observed in the Nyquist curves. R_s represents the resistance of the series components of the circuit, including the SBF. The constant phase element CPE_1, placed in parallel with the resistance R_1, is selected for the outer layer of the PEO coating. This combination accounts for both Faradaic- and non-Faradaic charge transfer and accumulation processes at the layer interfaces. Besides, the constant phase element is determined to achieve a better match of the experimental data with the circuit due to the porosity and surface roughness of the layers. Similarly, the constant phase element CPE_2, in parallel with the resistance R_2, represents the inner part of the PEO coating. The estimated data from the modeling are given in Table 3.

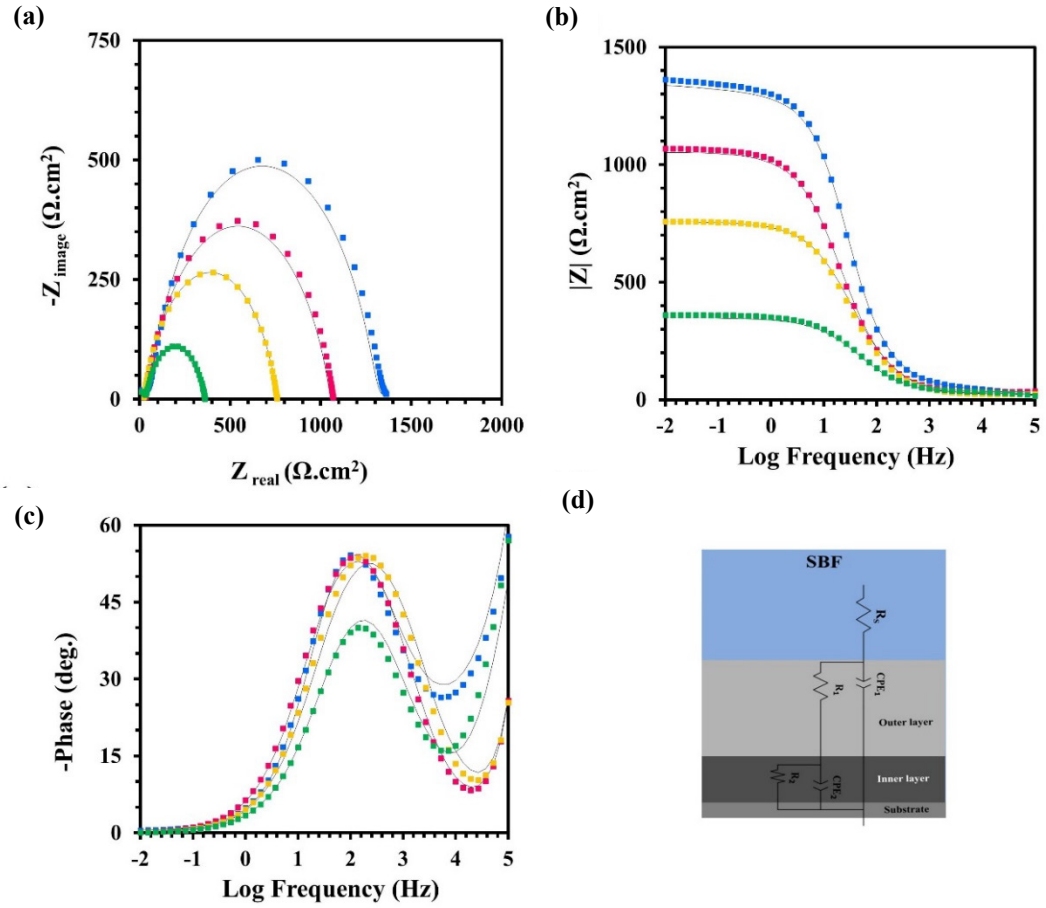

Figure 11. (a) Nyquist, (b) Bode modulus, (c) Bode phase of the samples, and (d) equivalent circuit

TABLE 3. The estimated EIS characteristics

Sample	R_s (Ω.cm²)	CPE_1 ($S^n.Ω^{-1}.cm^{-2}$)	n_1	R_1 (Ω.cm²)	CPE_2 ($S^n.Ω^{-1}.cm^{-2}$)	n_2	R_2 (Ω.cm²)
W0	22.2	2.09E-5	0.89	110.2	4.62E-5	0.79	1,319.9
W1.5	21.3	2.86E-5	0.86	95.6	6.30E-5	0.76	1,070.2
W3	27.8	3.10E-5	0.89	85.2	7.89E-5	0.73	737.1
W4.5	23.2	3.36E-5	0.75	39.1	7.95E-5	0.71	339.2

R_s, which is incluenced by the ionic strength of the SBF components, changes slightly. The values for the constant phase element of the inner and outer layers of the PEO coatings increase incrementally with the incorporation of wollastonite particles. The corresponding n values for both layers also deviate further from unity. These observations suggest that the incorporation of wollastonite particles introduces more inherent defects into the coatings and increase interfacial roughness. As the system deviates from the ideal capacitive behavior, charge transfer processes becomes more efficient, and degradation interactions occur at a faster rate.

The resistance of both outer and inner layers of the PEO coatings decreases, and reaches the lowest values of 39.1 and 339.2 Ω.cm² at W4.5 from 110.2 and 1,319.9 Ω.cm² at W0, respectively. This reduction in resistance results from the loss of compactness in both layers due to the formation of inherent defects. These defects facilitate the reach of deleterious species by creating multiple shortcuts in the movement pathway. The high destruction rate of wollastonite particles increases the sample's reactivity with the SBF (Córdoba-Torres et al., 2012; Orazem et al., 2006).

4. CONCLUSION

This work aimed to tune the bioactivity and degradation behavior of magnesium for use in biodegradable implants. In this regard, magnesium oxide coatings incorporated with different concentrations of wollastonite particles were created using the PEO process. The results revealed that composite layers with the characteristic PEO morphology were well formed. The presence of wollastonite particles significantly enhanced the bioactivity of the oxide layer, and this effect was further boosted by increasing the amount of the incorporated particles.

In addition, the embedment of wollastonite particles led to a decrease in the thickness and density of the PEO layer, though still slower than that of bare magnesium. These findings proved that upon adding wollastonite particles, the surface bioactivity and biodegradation properties of magnesium alloys can be tailored for different clinical conditions.

ACKNOWLEDGEMENTS

This research has been supported by grant No.: 247383 by Materials and Energy Research Center, Karaj, Iran.

REFERENCES

1. Bai, A., & Chen, Z. J. (2011). N, N, N′, N′-tetramethylethylenediamine on anticorrosion ability of micro-arc oxide coatings formed on magnesium alloy AZ91D. *Surface Engineering*, *27*(10), 790–795. https://doi.org/10.1179/026708410X12593178265869
2. Bordbar-Khiabani, A., Yarmand, B., & Mozafari, M. (2019). Enhanced corrosion resistance and in-vitro biodegradation of plasma electrolytic oxidation coatings prepared on AZ91 Mg alloy using ZnO nanoparticles-incorporated electrolyte. *Surface and Coatings Technology*, *360*. https://doi.org/10.1016/j.surfcoat.2019.01.002
3. Chen, Q., Kang, S., Li, Z., Tang, J. guo, Deng, Y., & Chen, M. an. (2024). Effect of changes in organo-silicon electrolyte concentration and composition on SiO2 ceramic coating prepared by plasma electrolytic oxidation on 6061 aluminum alloy. *Ceramics International*, *50*(17), 29920–29936. https://doi.org/10.1016/j.ceramint.2024.05.288
4. Córdoba-Torres, P., Mesquita, T. J., Devos, O., Tribollet, B., Roche, V., & Nogueira, R. P. (2012). On the intrinsic coupling between constant-phase element parameters α and Q in electrochemical impedance spectroscopy. *Electrochimica Acta*, *72*, 172–178. https://doi.org/10.1016/j.electacta.2012.04.020
5. Dehnavi, V., Luan, B. L., Liu, X. Y., Shoesmith, D. W., & Rohani, S. (2015). Correlation between plasma electrolytic oxidation treatment stages and coating microstructure on aluminum under unipolar pulsed DC mode. *Surface and Coatings Technology*, *269*(1), 91–99. https://doi.org/10.1016/j.surfcoat.2014.11.007
6. Erfanifar, E., Aliofkhazraei, M., Nabavi, H. F., & Rouhaghdam, A. S. (2017). Growth kinetics and morphology of microarc oxidation coating on titanium. *Surface and Coatings Technology*, *315*, 567–576. https://doi.org/10.1016/j.surfcoat.2017.03.002
7. Fattah-alhosseini, A., Chaharmahali, R., Babaei, K., Nouri, M., Keshavarz, M. K., & Kaseem, M. (2022). A review of effective strides in amelioration of the biocompatibility of PEO coatings on Mg alloys. *Journal of Magnesium and Alloys*, *10*(9), 2354–2383. https://doi.org/10.1016/j.jma.2022.09.002
8. Gnedenkov, S. V., Sinebryukhov, S. L., Mashtalyar, D. V., Imshinetskiy, I. M., Samokhin, A. V., & Tsvetkov, Y. V. (2015). Fabrication of coatings on the surface of magnesium alloy by plasma electrolytic oxidation using ZrO2 and SiO2 Nanoparticles. *Journal of Nanomaterials*, *2015*(1), 154298. https://doi.org/10.1155/2015/154298
9. Hussein, R. O., Nie, X., & Northwood, D. O. (2012). The application of plasma electrolytic oxidation (PEO) to the production of corrosion resistant coatings on magnesium alloys: A review. *Annual Conference of the Australasian Corrosion Association 2012*, *38*(1), 122–138. https://www.researchgate.net/publication/359068870
10. Ikonopisov, S. (1977). Theory of electrical breakdown during formation of barrier anodic films. *Electrochimica Acta*, *22*(10), 1077–1082. https://doi.org/10.1016/0013-4686(77)80042-X

11. Joo, S. Y., & Choe, H. C. (2025). Wollastonite-forsterite composite coatings containing Mn on the plasma electrolytic oxidized Ti-6Al-4V alloy via spin coating. *Surface and Coatings Technology*, *497*, 131797. https://doi.org/10.1016/j.surfcoat.2025.131797

12. Krishtal, M. M., Ivashin, P. V., Yasnikov, I. S., & Polunin, A. V. (2015). Effect of Nanosize SiO2 Particles Added into Electrolyte on the Composition and Morphology of Oxide Layers Formed in Alloy AK6M2 Under Microarc Oxidizing. *Metal Science and Heat Treatment*, *57*(7–8), 428–435. https://doi.org/10.1007/s11041-015-9900-8

13. Lu, X., Mohedano, M., Blawert, C., Matykina, E., Arrabal, R., Kainer, K. U., & Zheludkevich, M. L. (2016). Plasma electrolytic oxidation coatings with particle additions – A review. *Surface and Coatings Technology*, *307*, 1165–1182. https://doi.org/10.1016/j.surfcoat.2016.08.055

14. Mohedano, M., Arrabal, R., Mingo, B., Pardo, A., & Matykina, E. (2018). Role of particle type and concentration on characteristics of PEO coatings on AM50 magnesium alloy. *Surface and Coatings Technology*, *334*, 328–335. https://doi.org/10.1016/j.surfcoat.2017.11.058

15. Orazem, M. E., Pébère, N., & Tribollet, B. (2006). Enhanced Graphical Representation of Electrochemical Impedance Data. *Journal of The Electrochemical Society*, *153*(4), B129. https://doi.org/10.1149/1.2168377

16. Radha, R., & Sreekanth, D. (2017). Insight of magnesium alloys and composites for orthopedic implant applications – a review. *Journal of Magnesium and Alloys*, *5*(3), 286–312. https://doi.org/10.1016/j.jma.2017.08.003

17. Sedelnikova, M. B., Komarova, E. G., & Sharkeev, Y. P. (2016). Wollastonite and calcium phosphate biocoatings with Zn- and Cu-incorporation produced by a microarc oxidation method. *Key Engineering Materials*, *695*, 144–151. https://doi.org/10.4028/www.scientific.net/KEM.695.144

18. Sedelnikova, M. B., Ugodchikova, A. V., Tolkacheva, T. V., Chebodaeva, V. V., Cluklhov, I. A., Khimich, M. A., Bakina, O. V., Lerner, M. I., Egorkin, V. S., Schmidt, J., & Sharkeev, Y. P. (2021). Surface modification of mg0.8ca alloy via wollastonite micro-arc coatings: Significant improvement in corrosion resistance. *Metals*, *11*(5), 754. https://doi.org/10.3390/met11050754

19. Seetharaman, S., Sankaranarayanan, D., & Gupta, M. (2023). Magnesium-based temporary implants: potential, current status, applications, and challenges. *Journal of Functional Biomaterials*, *14*(6), 324. https://doi.org/10.3390/jfb14060324

20. Stern, M., A. L. G. (1957). Electrochemical Polarization: I . A Theoretical Analysis of the Shape of Polarization Curves. *Journal of The Electrochemical Society*, *104*(1), 56. https://doi.org/10.1149/1.2428496

21. Venkateswarlu, K., Rameshbabu, N., Sreekanth, S., Bose, A. C., Muthupandi, V., Babu, N. K., & Subramanian, S. (2012). Role of electrolyte additives on in-vitro electrochemical behavior of micro arc oxidized titania films on Cp Ti. *Applied Surface Science*, *258*(18), 6853–6863. https://doi.org/10.1016/j.apsusc.2012.03.118

22. Waizy, H., Seitz, J. M., Reifenrath, J., Weizbauer, A., Bach, F. W., Meyer-Lindenberg, A., Denkena, B., & Windhagen, H. (2013). Biodegradable magnesium implants for orthopedic applications. *Journal of Materials Science*, *48*(1), 39–50. https://doi.org/10.1007/s10853-012-6572-2

23. Witte, F. (2015). Reprint of: The history of biodegradable magnesium implants: A review. *Acta Biomaterialia*, *23*(S), S28–S40. https://doi.org/10.1016/j.actbio.2015.07.017

24. Xu, G., & Shen, X. (2019). Fabrication of SiO 2 nanoparticles incorporated coating onto titanium substrates by the micro arc oxidation to improve the wear resistance. *Surface and Coatings Technology*, *364*, 180–186. https://doi.org/10.1016/j.surfcoat.2019.01.069

25. Yang, C., Chen, P., Wu, W., Sheng, L., Zheng, Y., & Chu, P. K. (2024). A Review of Corrosion-Resistant PEO Coating on Mg Alloy. *Coatings*, *14*(4), 451. https://doi.org/10.3390/coatings14040451

26. Yerokhin, A. L., Leyland, A., & Matthews, A. (2002). Kinetic aspects of aluminium titanate layer formation on titanium alloys by plasma electrolytic oxidation. *Applied Surface Science*, *200*(1–4), 172–184. https://doi.org/10.1016/S0169-4332(02)00848-6

27. Yerokhin, A. L., Nie, X., Leyland, A., & Matthews, A. (2000). Characterisation of oxide films produced by plasma electrolytic oxidation of a Ti-6Al-4V alloy. *Surface and Coatings Technology*, *130*(2–3), 195–206. https://doi.org/10.1016/S0257-8972(00)00719-2